Volume 2 | Number 11 | November 2018

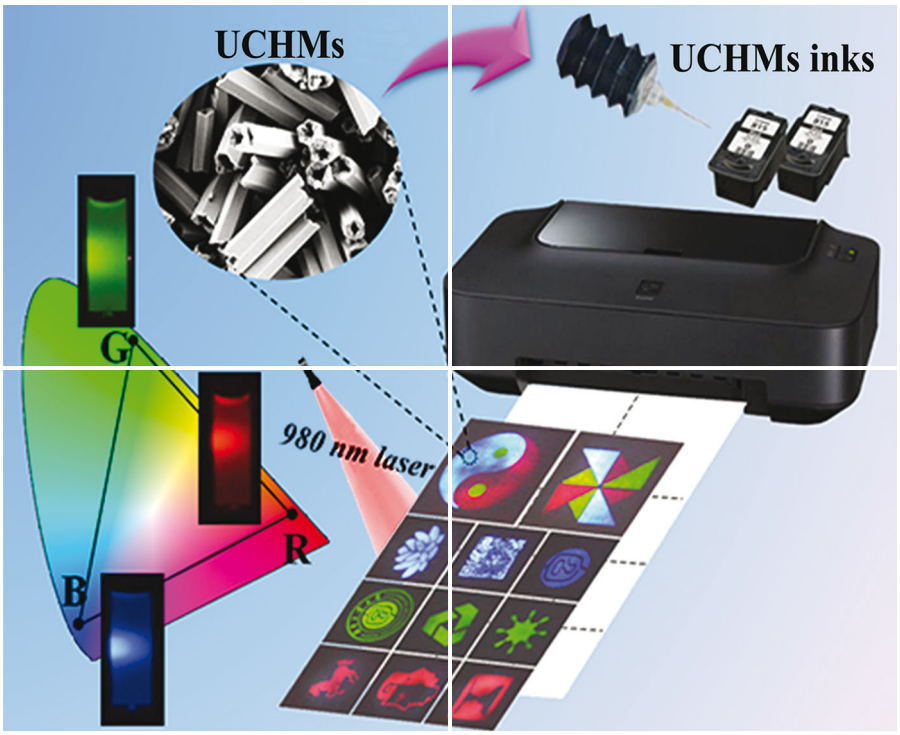

MATERIALS CHEMISTRY

FRONTIERS

Chinese Chemical Society
ROYAL SOCIETY OF CHEMISTRY
rsc.li/frontiers-materials

MATERIALS CHEMISTRY
FRONTIERS

RESEARCH ARTICLE

View Article Online
View Journal | View Issue

Cite this: *Mater. Chem. Front.*, 2018, **2**, 1997

Hydrothermal synthesis and inkjet printing of hexagonal-phase $NaYF_4$: Ln^{3+} upconversion hollow microtubes for smart anti-counterfeiting encryption†

Shaowen Xie,‡[ab] Chao Tong,‡[ab] Haihu Tan,[b] Na Li,[a] Liang Gong,[a] Jianxiong Xu,*[ab] Lijian Xu[a] and Changfan Zhang[ac]

Rational design and fabrication of well-defined upconversion phosphors are of great significance for anti-counterfeiting and security applications. Here, we present hydrothermal synthesis of novel upconversion hollow microtubes (UCHMs) composed of poly(acrylic acid) (PAA) functionalized hexagonal-phase $NaYF_4$: Ln^{3+}. The resulting UCHMs possess not only well-defined structures and uniform sizes, but also strong upconversion luminescence emission at room temperature. The structure–property relationship of the $NaYF_4$: Ln^{3+} crystal between the phase transition from cubic to hexagonal and morphological changes from nanospheres to hollow microtubes is obtained by detailed time-dependent experiments, which help to derive a possible growth mechanism of the UCHMs. Furthermore, by doping different lanthanide ions and tailoring the molar ratio of the doped lanthanide ions in the UCHMs, three-primary-color (RGB) UCHMs are successfully produced. The RGB UCHMs are fabricated into fluorescent inks by dispersal in a solvent mixture of ethanol, water, and glycerol. The resulting RGB UCHMs inks are inkjet printed on common paper to produce hidden images under ambient conditions. However, the hidden images can be read out with red-green-blue luminescence under 980 nm light excitation. The UCHMs-based inks enable the creation of light-responsive smart encryption patterns in a secure way, and such image encryption can be spatially and selectively printed on documents for anti-counterfeiting applications.

Received 14th June 2018,
Accepted 3rd July 2018

DOI: 10.1039/c8qm00278a

rsc.li/frontiers-materials

1. Introduction

Counterfeiting has a significant impact on fundamental research and industrial applications due to its threat to the global economy and human life.[1–3] The development of anti-counterfeiting technology is extremely critical for protecting intellectual property and detecting forged products in many applications. During the past few decades, a number of anti-counterfeiting technologies, including radio-frequency identification (RFID),[4] nuclear track technology,[5] and laser holograms[6] with the capacity of availability, authenticity and traceability, have been developed as a shield against counterfeiting. However, the preparation or detection of these anti-counterfeiting labels requires complex and expensive manufacturing equipment, and the stored information is easily rewritten.[7] Fluorescence-based optical anti-counterfeiting is considered as a promising technology due to its high fluorescence intensity, high stability against degradation, and ease of handling,[8] all of which greatly improve detection security.[9–14] Both organic and inorganic luminescent materials such as semiconductor quantum dots (QDs),[10] carbon dots,[11] and organic dyes[12,13] have been developed and used for anti-counterfeiting applications. These fluorescent materials are based on the so-called "down-conversion" mechanism, which can be readily excited to emit long-wavelength visible light using short-wavelength light (UV light). One classical example is to directly observe the anti-counterfeiting patterns on banknotes using a UV penlight. However, these downconversion fluorescent materials often suffer from photo-bleaching, high toxicity, broad emission bands, and ease of duplication, which greatly limit their uses for many applications.[14]

Different from downconversion fluorescent materials, upconversion materials as competitive alternatives that convert long-wavelength near-infrared (NIR) light to short-wavelength light (so-called anti-Stokes emission) through two-photon or

[a] *Hunan Key Laboratory of Biomedical Nanomaterials and Devices, College of Life Sciences and Chemistry, Hunan University of Technology, Zhuzhou 412007, P. R. China. E-mail: xujianxiong8411@163.com*
[b] *College of Packaging and Materials Engineering, Hunan University of Technology, Zhuzhou 412007, P. R. China*
[c] *College of Electrical and Information Engineering, Hunan University of Technology, Zhuzhou 412007, P. R. China*
† Electronic supplementary information (ESI) available. See DOI: 10.1039/c8qm00278a
‡ Joint first authors, contributed equally to this work.

multiphoton processes, possess many advantages such as being environmental benign, long fluorescence life, multicolor optical properties, and sharp emission bands.[15,16] These advantages make them useful for application in immunoassays,[17] fluorescence resonance energy transfer (FRET) sensors,[18] and displays.[19] Besides, the use of upconversion materials for anti-counterfeiting applications has great potential and advantages as compared to other materials.[20–22]

Upconversion phosphors, especially lanthanide ion-doped $NaYF_4$ ($NaYF_4$: Ln^{3+}), have been proven to be one of the most efficient phosphors for construction of visible upconversion luminescence films for anti-counterfeiting.[23–27] We recently reported the hydrothermal synthesis of water-dispersible branched $NaYF_4$: Yb^{3+}, Er^{3+} upconversion phosphors for preparation of a poly(vinyl alcohol) anti-counterfeiting film.[27] However, the difficulty in formation of a special pattern on the films appears to be less effective at preventing counterfeit goods. To address this issue, different technologies such as photolithography,[28] laser engraving,[29] screen printing,[30,31] and inkjet printing[32,33] have been developed to construct upconversion luminescent anti-counterfeiting labels with desirable patterns. Among these, inkjet printing using upconversion luminescent inks offers several advantages (*e.g.* high-throughput, low-cost, and easy designability) over others for anti-counterfeiting label fabrication.[32–36] Blumenthal *et al.* developed inks based on activated β-$NaYF_4$: Yb^{3+}, Er^{3+} nanocrystals to realize covert, monochrome, luminescent upconversion patterns.[32] Subsequently, Meruga *et al.* extended this study by the fabrication of multicolor two-dimensional codes using a new one-step printing process.[33] You *et al.* also used a thermal decomposition method to prepare highly efficient upconversion β-$NaYF_4$: Yb^{3+}, Tm^{3+}/Er^{3+} nanoparticles for fabricating anti-counterfeiting patterns *via* inkjet printing.[34] Recently, Ma *et al.* combined upconversion nanoparticles with commercial inkjet printers to develop a general, high throughput and easy-preparation method for background-free information encryption on paper.[35]

While anti-counterfeiting upconversion fluorescent patterns based on $NaYF_4$: Ln^{3+} crystals have been successfully printed, some limitations still remain regarding the existing inkjet printing technology. First, the preparation process of the above mentioned upconversion materials is complicated and dangerous, and requires high reaction temperatures and long reaction cycles (thermal decomposition method).[32–36] Second, the upconversion nanoparticles used in inkjet printing often suffer from low upconversion fluorescence due to the small sizes at the expense of weaker emissions.[37] In some cases, anti-counterfeit patterns have to be printed repeatedly several times and a laser with high excitation power has to be used to obtain visible fluorescence.[38] Additionally, due to the hydrophobic nature of the synthesized upconversion nanoparticles, polymer resin (poly(methyl methacrylate)[32,33] or poly(acrylic acid)[34]) and environmentally unfriendly organic solvents are often used to prepare printable fluorescent inks.[35]

To address the above challenges, herein we synthesized water-dispersible hexagonal-phase (β-phase) upconversion hollow microtubes (UCHMs) composed of poly(acrylic acid) (PAA) functionalized $NaYF_4$: Ln^{3+}, and then applied them in anti-counterfeiting *via* inkjet printing. The UCHMs were synthesized *via* a PAA assisted hydrothermal process. This method was mild and simple to use. The synthesized UCHMs exhibited strong upconversion fluorescence due to the pure hexagonal-phase with high crystallinity and the lower density of surface quenching centers of the microcrystal. Because of the strong upconversion fluorescence, the anti-counterfeit patterns can be obtained with one time printing under a laser of low excitation power, which is considered convenient and low cost. Moreover, the unique hollow structure and the PAA functionalized surface of the UCHMs endowed them with good dispersibility in water and made them suitable for formation of environment-friendly luminescent inks with high adhesion. By doping with different lanthanide ions and tailoring the molar ratio of the doped lanthanide ions, three-primary-color (RGB) UCHMs were obtained. The printable RGB UCHMs inks were formed by dispersing the as-obtained RGB UCHMs in a solvent mixture of ethanol, water and glycerol for fabricating anti-counterfeiting patterns *via* inkjet printing technology. This work demonstrates a new simple strategy to prepare environment-friendly luminescent inks with high upconversion fluorescence intensity for anti-counterfeiting applications.

2. Results and discussion

It is generally accepted that the properties of inorganic functional materials highly depend on their shape as well as size and composition. In particular, hollow structured materials, which have low density and high surface area have attracted much attention. It is demonstrated that $NaYF_4$: Ln^{3+} crystals with microtube shape possess higher fluorescence intensity than those with other morphologies (*e.g.*, cube, rod and prism).[39–42] Besides, the low density and high surface area of hollow microtubes endow them with good dispersibility in solvents. These make the $NaYF_4$: Ln^{3+} hollow microtubes a good candidate for preparation of fluorescent ink. Previous studies have shown that $NaYF_4$: Ln^{3+} hollow microtubes can be synthesized by a small molecular surfactant mediated hydrothermal method, using surfactants such as cetyltrimethyl ammonium bromide,[42] trisodium citrate,[43,44] ethylene diamine tetraacetic acid,[45] oleic acid,[46] *etc.* Herein, we chose PAA as the structure-directing agent for the sythesis of lanthanide ion-doped β-$NaYF_4$ hollow microtubes (UCHMs) *via* a hydrothermal process. PAA is a water-soluble anionic polymer containing a high concentration of carboxylic acid (COOH) groups, which can coordinate with the surface of the particles through functional groups of the polymer and render the hydrophilic nature of the synthesized $NaYF_4$: Ln^{3+} crystal. Moreover, the plenty of carboxylic acid groups are capable of forming interpolymer complexes *via* hydrogen bonding. The interpolymer complex of PAA yields a stronger adhesion, which is beneficial for the formulation of homogeneous UCHMs inks and printing on a paper substrate in our work.

2.1. Synthesis and characterization of UCHMs

2.1.1. Morphology, structure, and composition of the UCHMs. Lanthanide ion-doped β-$NaYF_4$ upconversion hollow microtubes

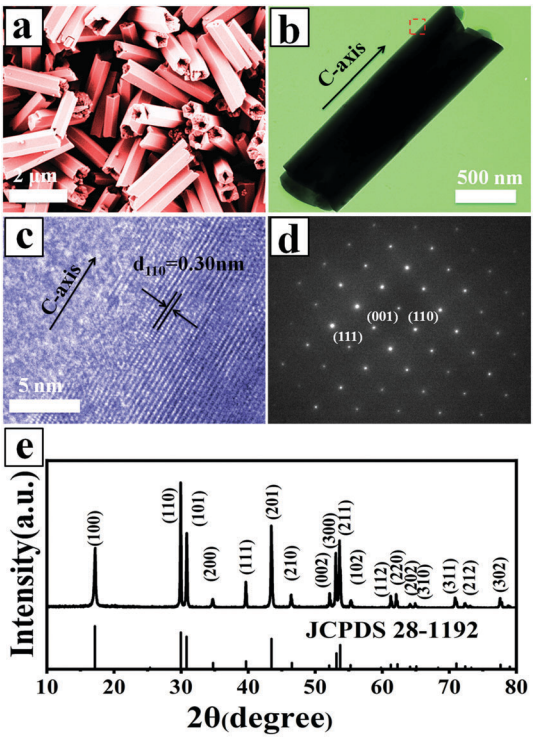

Fig. 1 (a) FE-SEM image of the UCHMs-G sample, (b) TEM image of a single UCHMs-G microtube, (c) HR-TEM image taken from the area marked by the red rectangle in part b, (d) the corresponding SAED pattern of the UCHMs-G and (e) XRD pattern of the UCHMs-G with the standard data of β-$NaYF_4$ (JCPDS No. 28-1192) as a comparison.

(UCHMs) were synthesized *via* a PAA assisted hydrothermal process with rare earth chlorides as lanthanide ion sources, and sodium fluoride as a sodium and fluoride source. As a proof-of-concept, the UCHMs-G prepared with the molar ratio of Y^{3+}, Yb^{3+}, Er^{3+} at 78 : 20 : 2 were selected to study their morphology, structure, and composition. Fig. 1a shows the morphology of the UCHMs-G as characterized by FE-SEM. It is seen from the FE-SEM image that a large quantity of hexagonal-prismatic microtubes with uniform sizes were clearly identified. All of the tubular structures had open ends, indicating the hollow structure of the microtubes. Fig. 1b shows the TEM image of an individual microtube. The length (L) and diameter (D) of the microtube were about 2.0 μm and 0.6 μm, respectively, resulting in an aspect ratio (L/D) of ~3.3 (Fig. 1 and Table 1).

From the symmetry of the morphology, the presence of hexagonal-prismatic microtubes implied the preferred direction of [0001] for a single tube to grow. The HRTEM image shows the high crystallinity of the obtained hexagonal-prismatic microtubes, with the interplanar distance of 0.30 nm corresponding to the (110) lattice plane of hexagonal-phase $NaYF_4$ (β-$NaYF_4$) (JCPDS No. 28-1192) (Fig. 1c). The selected area electron diffraction (SAED) pattern taken from the side of a microtube can be indexed as the (111), (001), and (110) planes of β-$NaYF_4$ (space group $P6_3/m$). The ordered hexagonal diffraction spots from the SAED pattern (Fig. 1d) demonstrated that the synthesized UCHMs-G exhibited a single crystalline feature. The XRD pattern of the UCHMs-G (Fig. 1e) resembled that of the standard pattern of pure β-$NaYF_4$ crystals (JCPDS No. 28-1192). No secondary phase was observed in the XRD pattern, revealing that Yb^{3+}/Er^{3+} ions were successfully doped into the β-$NaYF_4$ lattice. The ordered hexagonal diffraction spots in the SAED pattern, and sharp diffraction peaks in the XRD pattern collectively suggested that the synthesized UCHMs-G were pure β-$NaYF_4$: Ln^{3+} single crystals with high crystallinity. A phosphor with high crystallinity was critical for anti-counterfeiting applications, as it translated into less trap centers for photon emission and exhibited high luminescence.[47]

The element composition of the UCHMs-G was examined by EDXS. As shown in Fig. 2b, all the elements including Na, Y, F, Yb, and Er were detected in the EDXS spectrum. The molar ratio of Y: Yb: Er was 75.2 : 23.3 : 1.5, close to the feeding molar ratio of 78 : 20 : 2, as shown in the inset of Fig. 2b and Table 1. This confirmed that all of the rare earth metal elements were well-doped in the $NaYF_4$ matrix. The EDXS mapping (Fig. 2c–h) further showed that all the elements including the lanthanides were homogeneously distributed inside the UCHMs-G.

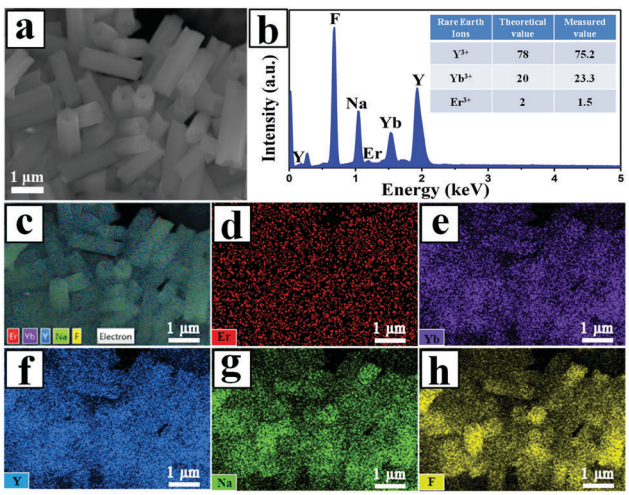

Fig. 2 (a) FE-SEM image of the UCHMs-G sample, (b) representative results of EDXS, (c) electron image and (d–h) Er, Yb, Y, Na and F elemental maps of the UCHMs-G, respectively.

Table 1 Morphology, structure, and composition of the RGB UCHMs

Samples (rare earth doping ions)	Phase	Morphology	L (nm)	D (nm)	Aspect ratios (L/D)	Rare earth ions composition	
						Theoretical molar ratio	Measured molar ratio
UCHMs-R (Y^{3+}, Er^{3+}, Tm^{3+})	Hexagonal	Hollow microtube	1350	400	3.375	88 : 10 : 2	86.8 : 10.7 : 2.5
UCHMs-G (Y^{3+}, Yb^{3+}, Er^{3+})	Hexagonal	Hollow microtube	2000	600	3.333	78 : 20 : 2	75.2 : 23.3 : 1.5
UCHMs-B (Y^{3+}, Yb^{3+}, Tm^{3+})	Hexagonal	Hollow microtube	1900	560	3.393	74.7 : 25 : 0.3	75.9 : 23.9 : 0.2

During the hydrothermal process, PAA polymers with pendant carboxyl groups can chelate with Ln^{3+} ions and were likely to bond onto the growing crystal surface. Therefore, PAA acted as both a capping ligand and a morphology control agent in our system. To demonstrate our assumption, a controlled experiment was carried out by synthesis of $NaYF_4$: Yb^{3+}, Er^{3+} upconversion phosphors (UCPs-G) without a capping ligand under the same experimental conditions. The chemical components of the UCHMs-G and UCPs-G were characterized by FTIR. Compared with the FTIR spectrum of the UCPs-G, some additional peaks were shown in the FTIR spectrum of the UCHMs-G (Fig. S1a, ESI†). Specifically, the peak at 2929 cm^{-1} was attributed to the methylene asymmetric C–H stretching vibrations of the long alkyl chain of PAA, the strong band at 1720 cm^{-1} was assigned to the C═O stretching vibration of the –COOH group, and the bands at 1583 and 1461 cm^{-1} were attributed to the carboxylate asymmetric and symmetric $–COO^-$ stretching in the PAA. The FTIR spectra (Fig. S1a, ESI†) and the difference in the dispersibilities of the UCHMs-G and UCPs-G in water (Fig. S1b, ESI†) demonstrate that the PAA polymers were indeed adhered onto the surface of the synthesized UCHMs-G. The XRD pattern of the UCPs-G showed that the synthesized UCPs-G were also pure β-$NaYF_4$: Ln^{3+} crystals. However, it should be pointed out that there is a large difference from each other in the relative intensities based on the (110) and (101) peaks for the UCPs-G and UCHMs-G (Fig. S1c, ESI†). This potentially suggested that the addition of the PAA capping ligand affected the possibility of different preferential growth orientations and therefore the morphology of the resultant $NaYF_4$: Ln^{3+} crystals. This was confirmed by the FE-SEM characterization. The synthesized UCPs-G have an irregular shape (Fig. S1d, ESI†), while the $NaYF_4$: Ln^{3+} crystals synthesized by employing PAA as a capping ligand exhibited a well-defined hollow structured microtube morphology (Fig. 1a).

2.1.2. Growth mechanism of the UCHMs. To examine the growth mechanism of the UCHMs, the time-dependent synthesis of UCHMs-G was performed under the same experimental conditions. The phase transformation and shape evolution of the intermediates were tracked by XRD and FE-SEM, respectively. Fig. 3 shows the XRD patterns of the intermediates obtained at different reaction time intervals. The intermediates displayed distinct XRD patterns at different reaction periods. Upon hydrothermal treatment for 1 h, a pure cubic phase $NaYF_4$ (α-$NaYF_4$) was first formed (Fig. 3a). When the reaction proceeded for 2 h, the stable hexagonal phase $NaYF_4$ (β-$NaYF_4$) emerged (Fig. 3b). Further reaction led to a dramatic increase of the fraction of β-$NaYF_4$, but a decrease of the α-$NaYF_4$ (Fig. 3c). The results suggested that the phase transformation from α-$NaYF_4$ to β-$NaYF_4$ occured through a dissolution-renucleation process. The diffraction peaks of the resultant crystal only appeared as a pure β-$NaYF_4$ at 24 h (Fig. 3d). These results indicated that the crystal growth evolved from cubic phase to mixed phase and ultimately to hexagonal phase as the reaction time was prolonged.

Fig. 4 shows a series of FE-SEM images that reveal the morphological evolution of the $NaYF_4$ crystals. As shown in Fig. 4a, the initial huge number of α-$NaYF_4$ spherical nanoparticles with an average diameter of 80 nm was formed in a short reaction

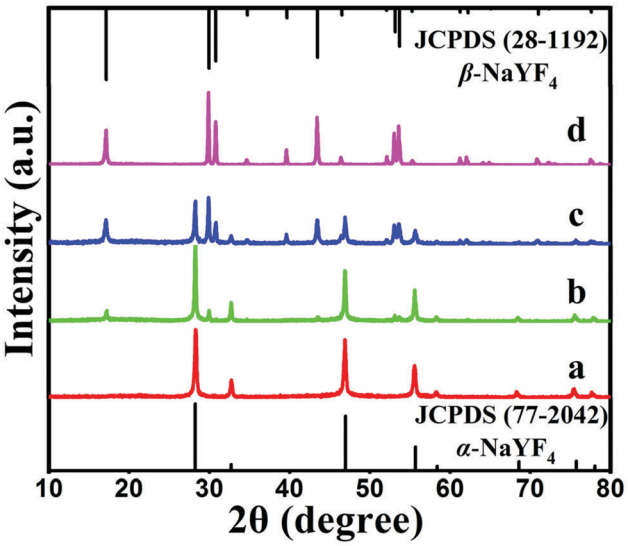

Fig. 3 XRD patterns of the intermediates obtained at different reaction time intervals: (a) 1 h, (b) 2 h, (c) 8 h and (d) 24 h, as well as the standard data of α-$NaYF_4$ (JCPDS No. 77-2042) and β-$NaYF_4$ (JCPDS No. 28-1192) phases for comparison.

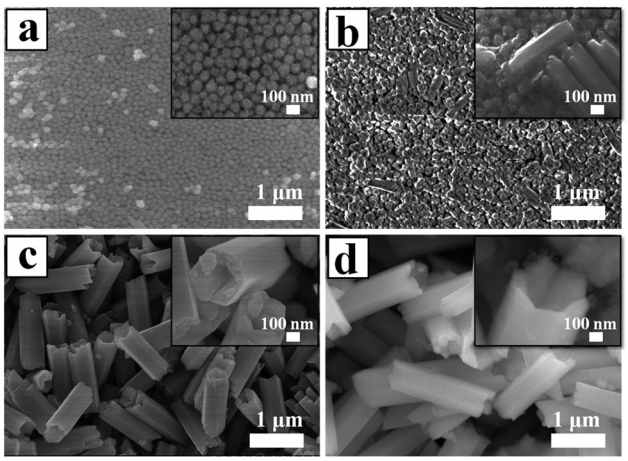

Fig. 4 The FE-SEM images of the intermediates obtained at different reaction time intervals: (a) 1 h, (b) 2 h, (c) 8 h and (d) 24 h. The insets represent the corresponding FE-SEM images at high magnification of each sample.

time (1 h). The well-defined spherical morphology of the nanoparticles was likely attributed to the isotropic unit cell structure of α-$NaYF_4$, resulting in an isotropic growth of the particles. It is well-known that the α-phase of $NaYF_4$ is a metastable thermodynamic state, during which these nanoparticles would serve as seeds for the growth of β-$NaYF_4$ hexagonal microrods *via* a dissolution-renucleation process under hydrothermal conditions.[48] This speculation was confirmed by the appearance of a few regular and well-defined microprisms in the intermediate products synthesized at 2 h of hydrothermal reaction (Fig. 4b). The average size of the observed microprisms was ~500 nm in length and ~150 nm in diameter, as shown in the inset of Fig. 4b. Moreover, a large amount of nanoparticles still co-existed with the intermediate product. XRD patterns also indicated that the co-existence of two shapes resulted from the presence of the

mixed crystal phase of α + β-$NaYF_4$. The formation of a hexagonal-shaped structure was due to the anisotropic unit cell structure of β-$NaYF_4$, which in turn induced anisotropic growth along a crystallographically reactive direction.[49] Therefore, different morphologies of the $NaYF_4$ products were attributed to α-$NaYF_4$ (nanoparticles) and β-$NaYF_4$ (microprisms). As the reaction time was increased to 8 h, the microprisms gradually became uniform and completely translated into microtubes, but a few small spherical solid particles were still observed. As shown in Fig. 4c, these microtubes were composed of six smooth lateral planes with reentrant grooves. The mean length and diameter of the microtubes were 1.4 μm and 0.4 μm, respectively. This suggested that the phase transition (α → β) and growth of β-$NaYF_4$ can directly induce the morphology change of $NaYF_4$ crystals from nanospheres to microprisms and further to microtubes.

After 24 h, the reaction yielded uniform microtubes with a 100% morphological yield and all of the tubular structures had open ends (Fig. 4d). The size of the microtubes increased from 1.4 μm to 2.0 μm in length and from 0.4 μm to 0.6 μm in diameter as the reaction time increased from 8 h to 24 h. Interestingly, the top end of the hexagonal prisms was not flat but like a crown as shown in the inset of Fig. 4d. Considering the dramatic growth of the $NaYF_4$ microtubes in the longitudinal direction and the microtubes with reentrant grooves synthesized at 8 h reaction, the resultant microtubes adopted hollow structures and pure hexagonal phase UCHMs-G.

Herein we propose a possible growth mechanism for UCHMs formation. In our protocol, the synthesis of the lanthanide ion-doped $NaYF_4$ microcrystals was developed by precipitating Na^+ and Ln^{3+} ions with fluorides in an aqueous solution. PAA polymers with pendant carboxyl groups were chelated with Ln^{3+} ions and designed to regulate the reaction by binding onto the growing crystal surface. At the beginning, PAA polymers formed complexes with Ln^{3+} ions (*i.e.* Ln^{3+}-PAA complexes) through strong coordination interactions. Under the hydrothermal condition of high temperature and high pressure, the chelating ability of the Ln^{3+}-PAA complexes became weaker, resulting in a gradual release of Ln^{3+} ions. The released Ln^{3+} ions would react with the Na^+ and F^- ions in solution to generate small $NaYF_4$ nuclei, as shown in Scheme 1, step I. Within a very short reaction time, these nuclei quickly congregated together and grew into α-$NaYF_4$ spherical nanoparticles. However, these α-$NaYF_4$ nanoparticles were thermodynamically unstable and then transformed into β-$NaYF_4$ seeds. Our FE-SEM and XRD results clearly show that the phase transformation (α → β) led to a dramatic morphology change due to the different characteristic unit cell structures in their crystallographic phases. The growth of β-$NaYF_4$ crystals generally follows the classical Ostwald ripening process in order to reduce the surface energy.[50] As the reaction time increased, anisotropic growth of the crystals became dominant by rapid dissolution of the α-$NaYF_4$ nanoparticles and release of monomers, and both effects resulted in the formation of β-$NaYF_4$ crystals. The dissolution-renucleation process of cubic-phase nanoparticles preferentially occured at the circumferential edges of each prism microrod along the crystallographically reactive direction, resulting in the formation of β-$NaYF_4$ microprisms with a well-defined cross section, as shown in Scheme 1, step II.

According to the general principle of crystal growth, the morphology of the crystals was correlated with the relative growth rate of different crystal facets.[51] The growth velocity in different crystallographic facets of β-$NaYF_4$ crystals were often influenced by two factors. The first factor was the coordination effect between F^- and Y^{3+} ions. Another factor was due to the selective adhesion of PAA ligands onto the specific crystal surface that in turn affected the kinetic morphology growth.[52] By calculating the electron localization function (ELF) in the $NaYF_4$ crystal (Fig. 5a and b), we identified a stronger bonding of Y^{3+} with F^- on the prismatic planes ({10$\bar{1}$0} crystal planes) than that on the top/bottom facets ({0001} crystal planes), due to the high density of Y^{3+} on the {10$\bar{1}$0} crystal planes as compared to the {0001} crystal planes. The high density of Y^{3+} also led to the higher capping ability of F^- ions on the prismatic facets than that of F^- ions on the top/bottom planes, which in turn decreased the average number of dangling bonds

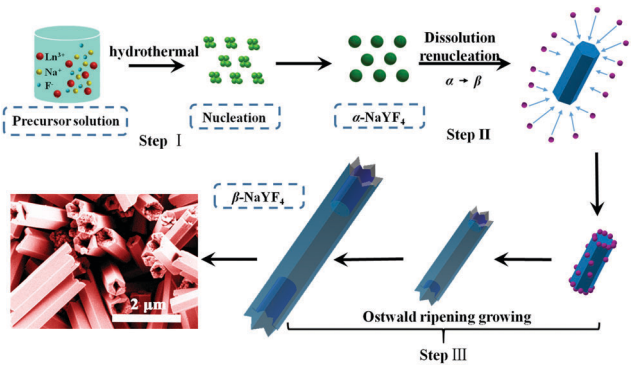

Scheme 1 Schematic illustration of the possible growth mechanism of UCHMs.

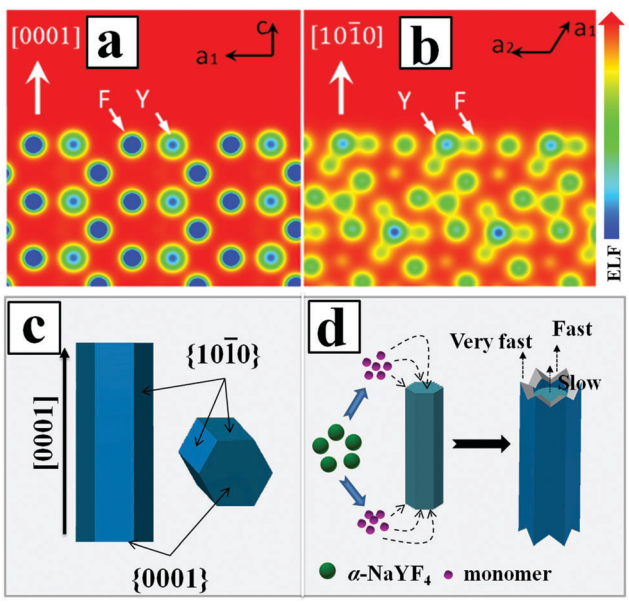

Fig. 5 Maps of the electron localization function (ELF) for (a) the {0001} facet and (b) the {10$\bar{1}$0} facet, (c) schematic presentation of the {0001} and {10$\bar{1}$0} facets of hexagonal phase $NaYF_4$ and (d) illustration of the formation of microtubes with hollow structures and crown-like top ends.

and further reduced the chemical potential of the crystal plane.[53] As a result, the growth rate along the [0001] direction was much faster than that along the [10$\bar{1}$0] direction. On the other hand, the high density of Y^{3+} on the {10$\bar{1}$0} crystal planes also induced more PAA ligands to be selectively adhered onto the crystal surface and thus inhibited the growth of {10$\bar{1}$0} crystal planes along the transverse direction. Meanwhile, the less adsorption of PAA ligands on the {0001} crystal planes resulted in a relatively faster growth rate along the [0001] direction than that along the [10$\bar{1}$0.] direction. Additionally, the growth of β-$NaYF_4$ microprisms consumed the vicinal monomers near rod-like $NaYF_4$ at the expense of the dissolution of nearby cubic α-$NaYF_4$ spherical-like particles. The dissolved monomers from cubic α-$NaYF_4$ will first be in contact with the extending top corner of the rods, followed by the rim and center area, leading to different growth rates at the top corner, rim, and center in the {0001} facet that eventually produced a hollow structure of $NaYF_4$ crystals with crown-like top ends, as shown in Fig. 5d.

2.1.3. Synthesis of three-primary-color UCHMs and their luminescence properties. The fluorescence property of the UCHMs-G was characterized by photoluminescence spectroscopy. Fig. 6a shows the upconversion emission spectrum of UCHMs-G as recorded from 400 to 700 nm under 980 nm laser excitation. Four major emission peaks were observed at 408, 525, 546, and 656 nm, corresponding to the transitions of $^2H_{9/2} \rightarrow {}^4I_{15/2}$, $^2H_{11/2} \rightarrow {}^4I_{15/2}$, $^4S_{3/2} \rightarrow {}^4I_{15/2}$, and $^4F_{9/2} \rightarrow {}^4I_{15/2}$ of Er^{3+}, respectively. Among these peaks, the green emission peaks were significantly higher than the other peaks. Consequently, a bright green upconversion emission was observed from the dispersion of the as-prepared UCHMs-G under 980 nm laser irradiation (Fig. 6a, inset image). Doping with different lanthanide ions induced different upconversion emissions under the irradiation of NIR light.[54] To prepare three-primary-color (RGB: red, green and blue) UCHMs, we tailored the luminescent properties of the UCHMs in red and blue emission by doping (10% Er^{3+}, 2% Tm^{3+}) and (25% Yb^{3+}, 0.3% Tm^{3+}) into the $NaYF_4$ matrix, respectively. The two samples were denoted as UCHMs-R and UCHMs-B. The structure, morphology, and composition of the UCHMs-R and UCHMs-B were examined by XRD, FE-SEM and EDXS, and the results are summarized in Fig. S2 (ESI†) and Table 1. As shown in Fig. S2 (ESI†), both UCHMs-R and UCHMs-B present similar hexagonal hollow microtube architectures. The molar ratios of lanthanide ions in the two samples were 86.8 : 10.7 : 2.5 (Y^{3+} : Er^{3+} : Tm^{3+}) and 75.9 : 23.9 : 0.2 (Y^{3+} : Yb^{3+} : Tm^{3+}), respectively, close to the feeding molar ratios in Table 1.

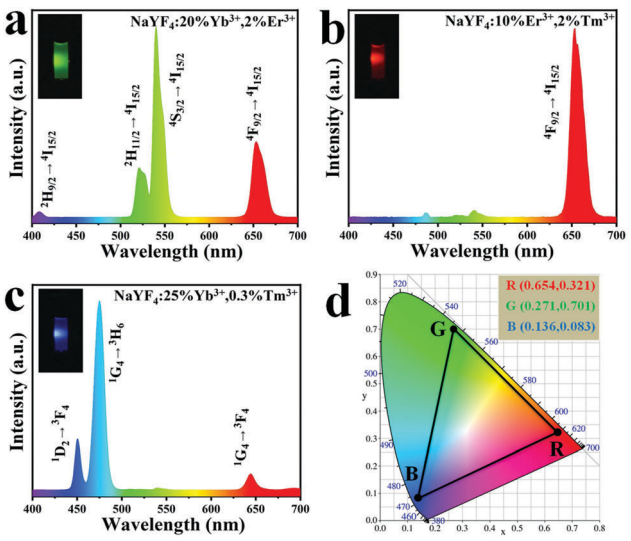

Fig. 6 The upconversion emission spectra of (a) UCHMs-G, (b) UCHMs-R, and (c) UCHMs-B (insets: the corresponding fluorescence images of RGB UCHMs dispersed in water obtained using a Nikon D7000 camera with an added infrared filter) and (d) the positions of the upconversion emission of RGB UCHMs within the CIE color coordinates.

The upconversion emission spectra of UCHMs-R and UCHMs-B are shown in Fig. 6b and c, respectively. In Fig. 6b, the major peak position of UCHMs-R is located at 656 nm of red color, corresponding to the transition of $^4F_{9/2} \rightarrow {}^4I_{15/2}$ of Er^{3+}. Thus, a bright red upconversion emission was observed from the dispersion of the as-prepared UCHMs-R under irradiation of a 980 nm laser (Fig. 6b, inset). For the UCHMs-B, divergent blue color emission peaks were located at 450 nm and 475 nm, while a red color emission peak was located at 644 nm. These three peaks corresponded to the $^1D_2 \rightarrow {}^3F_4$, $^1G_4 \rightarrow {}^3H_6$, and $^1G_4 \rightarrow {}^3F_4$ transitions of Tm^{3+}, respectively. Since the intensity of the blue emission peaks was significantly higher than that of the red peak, the UCHMs-B showed a blue color under the irradiation of a 980 nm laser (Fig. 6c, inset).

Furthermore, the fluorescence property of the RGB UCHMs in the solid state was examined using a confocal fluorescence microscope. As shown in Fig. S3 (ESI†), a high contrast, hypersensitive red, green, and blue fluorescent image of RGB UCHMs was observed at an excitation wavelength of 980 nm without auto-fluorescence from the background. The energy level diagrams of the Er^{3+}/Tm^{3+}, Yb^{3+}/Er^{3+} and Yb^{3+}/Tm^{3+} co-doped $NaYF_4$ lattice are shown in Fig. S4 (ESI†). The upconversion fluorescence of the RGB UCHMs was marked in the CIE color coordinates and is shown in Fig. 6d. The CIE color coordinates of the UCHMs-R, UCHMs-G, and UCHMs-B were (0.654, 0.321), (0.271, 0.701) and (0.136, 0.083), respectively. It can be seen that the triangle composed by the positions of the RGB UCHMs materials can cover almost half the region of the chromaticity diagram, which means that a variety of colors (including white) can be obtained based on the RGB UCHMs materials. In addition, it was demonstrated that all of the UCHMs exhibited stronger upconversion fluorescence than the upconversion nanoparticles (UCNPs) synthesized by an oleic acid assisted thermal decomposition method (Fig. S5, ESI†). This was due to the high crystallinity and the low density of surface quenching centers in the UCHMs microcrystals.[55] Overall, the hydrophilic property, unique morphology, strong upconversion fluorescence intensity and tunable fluorescence color made the UCHMs good fluorescent materials for inkjet printing for anti-counterfeiting applications.

2.2. Inkjet printing of UCHMs for anti-counterfeiting

While electronic communication has become an integral part of our daily life, paper still plays an indispensable role in

information storage, retrieval, and management systems. Many important documents, including passports, checks, and bonds, are paper-based. So, information encryption on paper is still a challenging task for many applications.[56,57] In this work, the as-prepared RGB UCHMs were dispersed in a solvent mixture of ethanol, water, and glycerol to form RGB fluorescent inks for anti-counterfeiting applications.

To ensure that the inks work stably in the inkjet printer, we tuned the ink properties by evaluating the printing performance (*i.e.*, dynamic viscosity and surface tension). Here we discuss the preparation of the UCHMs-G ink as a typical example. By fixing the weight ratio of UCHMs-G (0.2 wt%) and changing the weight ratio of deionized water, ethanol, and glycerol, a series of UCHMs-G inks were formulated (sample Ink1–Ink6). The detailed parameters of the preparation of Ink1–Ink6 are shown in Table S1 (ESI†). The properties of different UCHMs-G ink samples were characterized by evaluating the dynamic viscosity and surface tension, and the results are summarized in Table S2 (ESI†). Generally, the dynamic viscosity of ink can affect its flow in the cartridge and through the nozzle. High viscosity ink may cause the nozzle to clog, while low viscosity ink may cause damped oscillation and infiltration resulting in loss of print accuracy and luminescence intensity. In addition, an appropriate surface tension of ink helps in keeping a relatively small contact angle over the substrates, which increases the coverage area for a single drop of ink to form patterns with good uniformity under certain dots per inch (DPI) of a printer. The preferred dynamic viscosity and surface tension of ink for the inkjet printer may vary within a specific range at room temperature: the dynamic viscosity varies from 1 to 5 mPa s while the surface tension varies from 30 to 60 mN m^{-1}.[34,58] Based on the results in Table S2 (ESI†), we chose Ink5 as the optimized ink, where the dynamic viscosity and surface tension are 3.432 mPa s and 33.404 mN m^{-1}, respectively. By keeping the mass ratio of UCHMs-R (1.0 wt%) and UCHMs-B (0.5 wt%), respectively, another two upconversion fluorescent inks with proper dynamic viscosity and surface tension are prepared (Table S3, ESI†).

Multicolored and designable patterns were printed on the common A4 paper substrate using the as-obtained RGB fluorescent inks by inkjet printing technology. Scheme 2 shows the inkjet printing procedure of the UCHMs fluorescent inks on paper. During

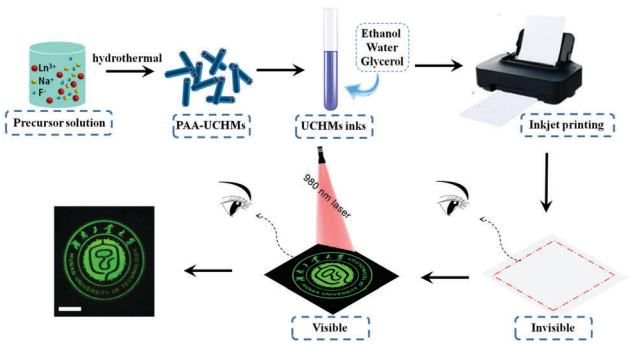

Scheme 2 Schematic of the inkjet printing of UCHMs for anti-counterfeiting applications.

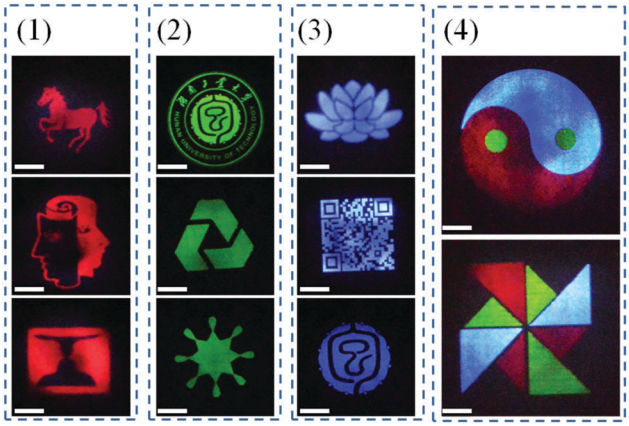

Fig. 7 Versatile optical micrographs of the inkjet printing patterns based on RGB UCHMs inks on an A4 paper substrate under 980 nm laser excitation: group (1) inkjet printing of red UCHMs inks, group (2) inkjet printing of green UCHMs inks, group (3) inkjet printing of blue UCHMs inks and group (4) inkjet printing of RGB UCHMs inks on the same layer (scale bar: 8 mm).

the first step, patterns were generated by independent deposition of RGB fluorescent inks on the A4 paper substrate. As shown in Fig. 7, under 980 nm light excitation, different printed patterns with different colors appeared on the paper with very fine details, including red patterns (horse, human face, and goblet patterns in Fig. 7, group 1), green patterns ("Hunan University of Technology" logo, triangle circle, and the star patterns in Fig. 7, group 2), and blue patterns (lotus, QR code, and the Chinese character of "㕣" which is the school badge of Hunan University of Technology in Fig. 7, group 3). Subsequently, the three-primary-color inks were printed as isolated and overlapping features to produce a more complicated images. As shown in (Fig. 7, group 4), colorful patterns of "taichi" diagram and windmill, which simultaneously emit distinct red, green and blue upconversion luminescence, can be observed under 980 nm light excitation. These images clearly indicate that the UCHMs ink-based anti-counterfeiting labels possessed excellent hiddenness and security, and could be used as a smart encryption for anti-counterfeiting and security applications.

3. Conclusions

Security of optical information is of great importance in modern society. In this work, novel β-$NaYF_4$ UCHMs doped with different lanthanide ions (Ln^{3+} = Er^{3+}/Tm^{3+}, Yb^{3+}/Er^{3+}, and Yb^{3+}/Tm^{3+}) were designed to produce red-green-blue luminescence using a facile hydrothermal process employing PAA as a stabilizing agent and ligand. The preparation of all the intermediates and the final products was simple and with high yields. All of the β-$NaYF_4$:Ln^{3+} UCHMs possessed well-defined structures and strong upconversion fluorescence. The formation of the $NaYF_4$ UCHMs involved a phase transition from pure cubic-phase to mixed cubic/hexagonal-phases to pure hexagonal-phase, correlating with morphology changes from spherical nanoparticles to short microprisms, and ultimately to hollow microtubes. Both the

phase transitions and morphology changes were attributed to the classical Ostwald ripening process and different growth rates of different crystal facets. More importantly, upon doping of UCHMs with different lanthanide ions and tailoring the molar ratio of the doped lanthanide ions, three-primary-color (RGB) UCHMs were prepared. The resulting RGB UCHMs can be dispersed in a solvent mixture of ethanol, water, and glycerol to obtain different fluorescent inks. We further demonstrated that the RGB UCHMs inks can be used to print hidden optical images on regular paper using inkjet printing technology. These hidden images were completely invisible at standard lighting conditions, but became visible with multi-luminescent colors at 980 nm light excitation. We envision that the environment-friendly UCHMs fluorescent inks, integrating their simple fabrication process, rapid inkjet printing, and difficulty for encryption, have enormous potential for anti-counterfeiting, multilevel image encryption, and background-free image reconstruction.

Conflicts of interest

There are no conflicts to declare.

Acknowledgements

The financial support by National Key Research and Development Program of China (2018YFD0400705), National Science Foundation of China (21501056 and 21705043), the National Science Foundation for Post-Doctoral Scientists of China (2018M632981), and the Science Foundation of Hunan Province (218JJ3115 and 218JJ3117) is gratefully acknowledged.

Notes and references

1 T. Kelesidis, I. Kelesidis, P. I. Rafailidis and M. E. Falagas, *J. Antimicrob. Chemother.*, 2007, **60**, 214–236.
2 B. Yoon, J. Lee, I. S. Park, S. Jeon, J. Lee and J. M. Kim, *J. Mater. Chem. C*, 2013, **1**, 2388–2403.
3 K. Pawan, S. Satbir and K. G. Bipin, *Nanoscale*, 2016, **8**, 14297–14340.
4 A. Mitrokotsa, M. R. Rieback and A. S. Tanenbaum, *Inf. Syst. Front.*, 2009, **12**, 491–505.
5 T. Zhang, L. Fu, Z. Chen, Y. Cui and X. Liu, *Prog. Org. Coat.*, 2016, **100**, 100–104.
6 H. Peng, S. Bi, M. Ni, X. Xie, Y. Liao, X. Zhou, Z. Xue, J. Zhu, Y. Wei, C. N. Bowman and Y. W. Mai, *J. Am. Chem. Soc.*, 2014, **136**, 8855–8858.
7 W. Yao, Q. Tian, J. Liu, Q. Xue, M. Li, L. Liu, Q. Lu and W. Wu, *Nanoscale*, 2017, **9**, 15982–15989.
8 J. Andres, R. D. Hersch, J. E. Moser and A. S. Chauvin, *Adv. Funct. Mater.*, 2014, **24**, 5029–5036.
9 Z. Xu, D. Gonzalez-Abradelo, J. Li, C. A. Strassert, B. J. Ravoo and D. S. Guo, *Mater. Chem. Front.*, 2017, **1**, 1847–1852.
10 X. Wu, H. Liu, J. Liu, K. N. Haley, J. A. Treadway, J. P. Larson, N. Ge, F. Peale and M. P. Bruchez, *Nat. Biotechnol.*, 2003, **21**, 41–46.
11 M. You, M. Lin, S. Wang, X. Wang, G. Zhang, Y. Hong, Y. Dong, G. Jin and F. Xu, *Nanoscale*, 2016, **8**, 10096–10104.
12 A. H. Mady, M. L. Baynosa, D. Tuma and J. J. Shim, *Appl. Catal., B*, 2017, **203**, 416–427.
13 J. Liu, Y. Zhuang, L. Wang, T. Zhou, N. Hirosaki and R. J. Xie, *ACS Appl. Mater. Interfaces*, 2018, **10**, 1802–1809.
14 X. Liu, R. Deng, Y. Zhang, Y. Wang, H. Chang, L. Huang and X. Liu, *Chem. Soc. Rev.*, 2015, **44**, 1479–1508.
15 F. Wang and X. Liu, *Acc. Chem. Res.*, 2014, **47**, 1378–1385.
16 J. Cheng, E. H. Hill, Y. Zheng, T. He and Y. Liu, *Mater. Chem. Front.*, 2018, **2**, 662–678.
17 M. You, Z. Li, P. Zhang, D. Bai, M. Lin and F. Xu, in *Handbook of Immunoassay Technologies*, ed. S. K. Vashist and J. H. T. Luong, Academic Press, 2018, pp. 273–304, DOI: 10.1016/B978-0-12-811762-0.00011-6.
18 B. Jin, S. Wang, M. Lin, Y. Jin, S. Zhang, X. Cui, Y. Gong, A. Li, F. Xu and T. J. Lu, *Biosens. Bioelectron.*, 2017, **90**, 525–533.
19 B. Zhu, B. Qian, Y. Liu, C. Xu, C. Liu, Q. Chen, J. Zhou, X. Liu and J. Qiu, *NPG Asia Mater.*, 2017, **9**, e394.
20 M. Hu, D. Ma, C. Liu, J. Wang, Z. Zhang and L. Meng, *J. Mater. Chem. C*, 2016, **4**, 6975–6981.
21 A. Baride, J. M. Merug, C. Douma, D. Langerman, G. Crawford, J. J. Kellar, W. M. Crossb and P. S. May, *RSC Adv.*, 2015, **5**, 101338–101346.
22 G. P. Darshan, H. B. Premkumar, H. Nagabhushana, S. C. Sharma, S. C. Prashantha, H. P. Nagaswarup and B. D. Prasad, *Dyes Pigm.*, 2016, **131**, 268–281.
23 B. Zhou, B. Shi, D. Jin and X. Liu, *Nat. Nanotechnol.*, 2015, **10**, 924–936.
24 X. Sang, W. Chen, P. Chen, X. Liu and J. Qiu, *J. Mater. Chem. C*, 2015, **3**, 9089–9094.
25 J. C. Boyer, N. J. J. Johnson and F. C. J. M. v. Veggel, *Chem. Mater.*, 2009, **21**, 2010–2012.
26 R. Chai, H. Lian, Z. Hou, C. Zhang, C. Peng and J. Lin, *J. Phys. Chem. C*, 2010, **114**, 610–616.
27 H. Tan, S. Xie, J. Xu, N. Li, C. Zhang, L. Xu and J. Zheng, *Sci. Adv. Mater.*, 2017, **9**, 2223–2233.
28 Y. Liu, Y. H. Lee, Q. Zhang, Y. Cui and X. Y. Ling, *J. Mater. Chem. C*, 2016, **4**, 4312–4319.
29 M. Ecker and T. Pretsch, *RSC Adv.*, 2014, **4**, 286–292.
30 M. Li, W. Yao, J. Liu, Q. Tian, L. Liu, J. Ding, Q. Xue, Q. Lu and W. Wu, *J. Mater. Chem. C*, 2017, **5**, 6512–6520.
31 L. He, L. Xia, Y. Yang, Q. Zheng, N. Jiang, C. Xu, Y. Liu and D. Lin, *Mater. Res. Bull.*, 2017, **95**, 483–490.
32 T. Blumenthal, J. Meruga, P. Stanley May, J. Kellar, W. Cross, K. Ankireddy, S. Vunnam and Q. N. Luu, *Nanotechnology*, 2012, **23**, 185305–185312.
33 J. M. Meruga, A. Baride, W. Cross, J. J. Kellar and P. S. May, *J. Mater. Chem. C*, 2014, **2**, 2221–2227.
34 M. You, J. Zhong, Y. Hong, Z. Duan, M. Lin and F. Xu, *Nanoscale*, 2015, **7**, 4423–4431.
35 Q. Ma, J. Wang, Z. Li, D. Wang, X. Hu, Y. Xu and Q. Yuan, *Inorg. Chem. Front.*, 2017, **4**, 1166–1172.
36 L. L. da Luz, R. Milani, J. F. Felix, I. R. Ribeiro, M. Talhavini, B. A. Neto, J. Chojnacki, M. O. Rodrigues and S. A. Junior, *ACS Appl. Mater. Interfaces*, 2015, **7**, 27115–27123.

37 W. Gao, H. Zheng, Q. Han, E. He and R. Wang, *CrystEngComm*, 2014, **16**, 6697–6706.
38 G. Bühler and C. Feldmann, *Appl. Phys. A: Mater. Sci. Process.*, 2007, **87**, 631–636.
39 M. Ding, D. Chen, S. Yin, Z. Ji, J. Zhong, Y. Ni, C. Lu and Z. Xu, *Sci. Rep.*, 2015, **5**, 12745–12757.
40 M. Lin, Y. Zhao, M. Liu, M. Qiu, Y. Dong, Z. Duan, Y. Li, B. Pingguan-Murphy, T. Lu and F. Xu, *J. Mater. Chem. C*, 2014, **2**, 3671–3676.
41 C. Li, Z. Quan, P. Yang, S. Huang, H. Lian and J. Lin, *J. Phys. Chem. C*, 2008, **112**, 13395–13404.
42 Y. Su, L. Li and G. Li, *Cryst. Growth Des.*, 2008, **8**, 2678–2683.
43 B. Chen, W. Kong, Y. Liu, Y. Lu, M. Li, X. Qiao, X. Fan and F. Wang, *Angew. Chem., Int. Ed.*, 2017, **56**, 10383–10387.
44 D. Gao, D. Tian, X. Zhang and W. Gao, *Sci. Rep.*, 2016, **6**, 22433–22442.
45 B. Chen, T. Sun, X. Qiao, X. Fan and F. Wang, *Adv. Opt. Mater.*, 2015, **3**, 1577–1581.
46 S. Zeng, G. Ren, W. Li, C. Xu and Q. Yang, *J. Phys. Chem. C*, 2010, **114**, 10750–10754.
47 F. Shi, J. Wang, D. Zhang, G. Qin and W. Qin, *J. Mater. Chem.*, 2011, **21**, 13413–13421.
48 X. Guo, P. Li, S. Yin and W. Qin, *J. Fluorine Chem.*, 2017, **200**, 91–95.
49 S. Ullah, C. Hazra, E. P. Ferreira-Neto, T. C. Silva, U. P. Rodrigues-Filho and S. J. L. Ribeiro, *CrystEngComm*, 2017, **19**, 3465–3475.
50 M. Ding, Y. Li, D. Chen, H. Lu, J. Xi and Z. Ji, *J. Alloys Compd.*, 2016, **658**, 952–960.
51 M. K. Singh and A. Banerjee, *Cryst. Growth Des.*, 2013, **13**, 2413–2425.
52 Y. Yin and A. P. Alivisatos, *Nature*, 2005, **437**, 664–670.
53 X. Liang, X. Wang, J. Zhuang, Q. Peng and Y. Li, *Adv. Funct. Mater.*, 2007, **17**, 2757–2765.
54 H. Dong, L. D. Sun and C. H. Yan, *Chem. Soc. Rev.*, 2015, **44**, 1608–1634.
55 F. Wang, J. Wang and X. Liu, *Angew. Chem., Int. Ed.*, 2010, **49**, 7456–7460.
56 W. Jeong, M. I. Khazi, D. H. Park, Y. S. Jung and J.-M. Kim, *Adv. Funct. Mater.*, 2016, **26**, 5230–5238.
57 W. Wang, N. Xie, L. He and Y. Yin, *Nat. Commun.*, 2014, **5**, 5459–5465.
58 B. J. de Gans and U. S. Schubert, *Macromol. Rapid Commun.*, 2003, **24**, 659–666.